Burnout susceptibility of silicon power diodes when exposed to 14 MeV neutrons

G. Canale Parola, *Graduate Student Member, IEEE*, S. Palazzo, *Member, IEEE*, G. Busatto, *Member, IEEE,* A. Sanseverino, *Member, IEEE*, E. Martano, S.G. Alberton, J. Wyss, and F. Velardi *Member, IEEE*.

Abstract— **Neutrons can lead to significant failures in high-voltage power devices; this paper investigates the behavior of a silicon-power PiN diode when exposed to a 14 MeV neutron beam. We present a novel methodology that combines experimental characterization and numerical simulation to examine the effects of ionic species generated by neutron-induced nuclear reactions in semiconductor materials. Experimental measurements were conducted at the Frascati Neutron Generator to explore the device's failure under controlled irradiation conditions. Subsequently, to comprehend the failure mechanism, a combined simulation approach was adopted. The G4SEE Monte Carlo toolkit was first employed to simulate the interaction of 14 MeV neutrons with the silicon semiconductor material; the resulting secondary particle data were then utilized in three-dimensional electrothermal simulations performed using Silvaco TCAD, leveraging the cylindrical symmetry of the unit cell. The numerical model was validated by comparing the simulation results with the experimental data obtained during the neutron irradiation campaigns. Our study revealed that the (α, ^{25}Mg) ion pair is one of the products of the nuclear reaction that interacts most significantly with the electric field within the intrinsic region of the device. This interaction at the critical bias voltage results in a single-event burnout of the diode, as confirmed by experimental observations and numerical analysis. Although the demonstration is based on a monoenergetic 14 MeV source, the methodology is general and can be extended to assess device response under realistic atmospheric neutron spectra.**

***Index Terms*—Neutron Beams Irradiation, Silicon PiN Diodes, Single Event Burnout, TCAD Electrothermal Simulations.**

I. Introduction

COSMIC rays, originating both from the Sun and from sources outside the solar system, continuously bombard the Earth. When these high-energy particles interact with the terrestrial atmosphere, they generate cascades of secondary particles, including neutrons, protons, electrons, muons, pions, gamma rays, and heavy nuclei. Among these products, neutrons are widely recognized as the most significant threat to the reliability of power electronics at ground level and at avionics altitudes [1, 2]. At sea level, the neutron spectrum is continuous and decreases with energy, extending from thermal energies up to several 1 GeV. These neutrons are the primary contributors to single event effects (SEEs) in semiconductor devices [3 - 9], with Single-Event Burnout (SEB) being a critical failure mode for high-voltage power devices [2, 5, 10, 11, 12, 13].

Approximately half of the fast neutron flux (E > 1 MeV) lies in the 1–20 MeV energy range, making this interval particularly relevant for terrestrial reliability studies. Although the flux of fast neutrons at sea level is relatively low (~21 n cm^{-2} hr^{-1}), the ubiquity of electronic devices makes neutron SEE testing essential for evaluating their reliability in terrestrial environments [11].

Terrestrial neutrons interact with the atomic nuclei in the materials that make up a device, producing secondary particles via inelastic scattering or nuclear reactions. When these particles deposit sufficient ionization, they can trigger Single-Event Burnout (SEB) by inducing a localized high-current pulse. The experimental characterization of neutron-induced SEEs is typically carried out either by exposing many devices to the natural neutron flux or at irradiation facilities using neutrons with spectra similar to the terrestrial environment. These procedures assess the reliability degradation of the Devices Under Test (DUTs) they often lack the granularity required to isolate specific failure mechanisms driven by distinct nuclear reaction channels. The authors in [10] present a predictive model that focuses solely on the recoil particle resulting from the nuclear reaction, without considering the entire reaction channel. However, for low energy neutrons, the contribution of the ejectile is crucial to triggering the failure mechanism and should not be neglected.

We propose a methodology to identify the reaction channel resulting from the interaction of the neutrons with the semiconductor material, which causes the failure of the device. The methodology combines experimental data with finite element electrothermal simulations, starting from the energies of the secondary particles calculated using a Monte Carlo kinematic numerical analysis.

The irradiation campaign was conducted at the Frascati Neutron Generator (FNG) [14]. Unlike pulsed spallation sources, the FNG is an accelerator-driven source operating in continuous wave mode, providing a steady flux of 14 MeV neutrons. This facility produces 14 MeV neutrons via the deuterium-tritium reaction:

$$^{2}D + {}^{3}T \rightarrow {}^{4}He + n \quad (1)$$

commonly denoted as D(T,n)α. This specific energy allows for the study of threshold reactions and ionization effects that are otherwise averaged out in broad-spectrum sources [9, 13].

G. Canale Parola, S. Palazzo, G. Busatto, A. Sanseverino, E. Martano, and F. Velardi are with the Department of Electrical and Information Engineering, University of Cassino and Southern Lazio, Italy (e-mail: giovanni.canaleparola@unicas.it; simone.palazzo@unicas.it; busatto@unicas.it; a.sanseverino@unicas.it; emanuele.martano@unicas.it; velardi@unicas.it).

Saulo G. Alberton is with the Instituto de Fisica, Universidade de Sao Paulo, Brazil, and also with the Instituto de Fisica "Gleb Wataghin", Universidade Estadual de Campinas, Brazil (e-mail: alberton@if.usp.br).

Jeffery Wyss is with the Department of Civil and Mechanical Engineering, University of Cassino and Southern Lazio, Italy, and also with the National Institute of Nuclear Physics of Padua, Italy (e-mail: wyss@unicas.it).

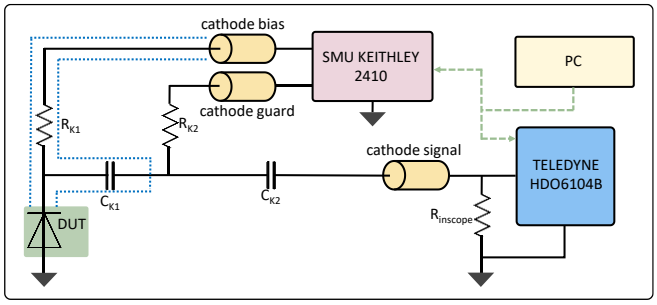

Fig. 1. The schematic of the experimental setup.

In this work, six 600 V-rated silicon PiN power diodes were tested. During each irradiation, the current pulses generated by nuclear reactions at the device terminals were recorded under different reverse bias conditions until the SEB event occurred.

The G4SEE Monte Carlo toolkit [15] was employed to simulate the interaction of 14 MeV neutrons with the silicon semiconductor material. This allowed for the detailed identification of the secondary ion species such as:

$$^{28}Si + n \rightarrow {}^{28}Al + p \; and \; {}^{30}Si + n \rightarrow {}^{25}Mg + \alpha \qquad (2)$$

and the calculation of their Linear Energy Transfer (LET) distributions and kinetic energies.

The output from G4SEE provided the physical inputs for the Silvaco-TCAD simulator [16], which was then used to model the electrical and thermal response of the device to these specific ionization events. This methodology facilitates a direct correlation between the experimentally observed current pulses and the specific nuclear reactions most likely to induce damage.

These findings provide insights into the mechanisms of SEB in silicon PiN diodes under neutron irradiation, advancing the understanding of radiation-induced failures.

II. The Experiment Set-Up

The schematic of the circuit used for the experiments is shown in Fig. 1. The device under test (DUT) is reverse-biased through a constant voltage supplied via the Source Measure Unit (SMU), Keithley 2410, which simultaneously measures the cathode leakage current during neutron irradiation. The instrument is capable of sourcing voltages up to 1100 V and measuring currents with a maximum limit of 105 µA. The SMU was connected to the test circuit through triaxial cables to limit the leakage currents to a minimum, which could otherwise affect the accuracy of the measurement.

The diode cathode was connected to a TELEDYNE Lecroy HDO6104B high-resolution oscilloscope (1GHz, 10GS/s) via a triaxial cable. The oscilloscope input was configured with unity attenuation and set to high impedance (1 MΩ) to protect the instrument from potential over-voltages in the event of a breakdown of the irradiated DUT. Additionally, a resistor $R_{inscope}$ was placed directly at the oscilloscope input to convert the current pulses, generated by neutron interactions with the semiconductor material, into a voltage signal.

The cables employed to connect the test circuit to the measurement instrumentation were BELDEN 9222, featuring a 50 Ω characteristic impedance to maintain impedance matching with the circuit. Each cable was 12 m long and had an attenuation of 0.75 dB/m over a bandwidth of 1 GHz. The use of triaxial cabling was essential to minimize coupling effects and external noise. A guard ring was placed on the circuit board close to the cathode bias line, with the guard line held at the same potential as the respective bias line to minimize the leakage current. The test circuit includes capacitors and resistors in the cathode mesh for biasing the DUT and coupling it to the oscilloscope. All capacitance and resistance values are reported in Table I.

TABLE I
EXPERIMENTAL CIRCUIT DETAILS

Symbol	Value	Unit
C_{K1}	10	µF
C_{K2}	470	nF
R_{K1}	1	MΩ
R_{K2}	30	kΩ
$R_{inscope}$	50	Ω

The capacitors have a parasitic resistance that can significantly contribute to leakage currents, thereby reducing the accuracy of measurements of radiation induced variations in the DUT. To limit the leakage current through these capacitors, they were split into two components: C_{K1} and C_{K2}, with rated voltages of 50 V and 1000 V, respectively.

Moreover, a guard ring surrounds C_{K1}, with its potential maintained at 0 V by a resistor R_{K2}. Consequently, the series combination of the two capacitors can withstand voltages up to 1 kV. This voltage is primarily sustained by C_{K2} due to its significantly lower capacitance compared to C_{K1}; furthermore, under static polarization conditions, the potential difference across C_{K1} is negligible. This configuration effectively nullifies the contribution of the biasing capacitor to the leakage current.

A resistor R_{K1} is placed in series between the DUT and the Keithley 2410 to increase the impedance of the cathode bias line, enabling the oscilloscope to capture the current pulses from neutron-induced nuclear reactions. The large time constant $R_{K1} \cdot C_{K1}$ slows the relaxation of the biasing voltage. To expedite stabilization of the cathode voltage V_K before the irradiation, a relay temporarily bypasses R_{K1}. Furthermore, the relay isolates the oscilloscope sensing branch during the acquisition of the cathode leakage current characteristics before and after irradiation. The sample holder consists of a printed circuit board (PCB) enclosed in an aluminum parallelepiped with 2-mm-thick side walls and base. The thickness of the remaining surface, through which the diode is irradiated, is 0.5 mm. The aluminum structure acts as a Faraday cage, preventing interference from the electromagnetic fields generated by the neutron source in the radiation hall.

III. The Experimental Procedure

Commercial 600 V, 30 A silicon PiN diodes manufactured by ON Semiconductor (RURG3060-F085), were irradiated at the ENEA center's Frascati Neutron Generator (FNG).

The FNG is a linear electrostatic accelerator that produces 14 MeV neutrons through the nuclear fusion of deuterium and tritium [17, 18]. The source operates in continuous wave mode, delivering a steady and constant neutron flux. Both reagents are hydrogen isotopes: deuterium has one neutron in addition to the proton, while tritium contains two. Since fusion requires an initial energy input to overcome the Coulomb barrier, the

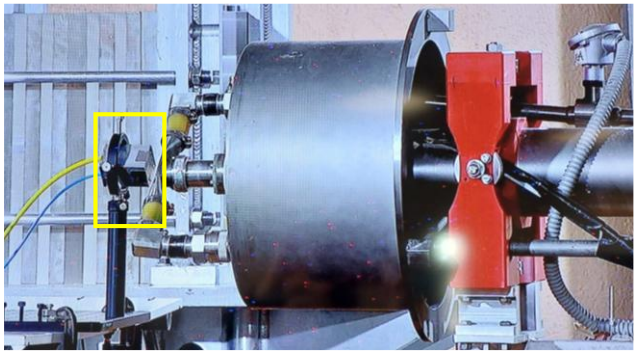

Fig. 2. The neutron source and the sample holder in the yellow rectangle.

accelerator boosts deuterium ions to an energy of 0.3 MeV, providing them with sufficient energy to continuously collide with a tritiated titanium target and initiate the reaction [17]. The accelerator is housed in a large shielded hall, with the target located over four meters from the walls, floor, and ceiling. These dimensions were chosen to reduce neutron reflections and to keep the moderated/thermalized neutron background at very low levels.

The FNG generates one of the most intense neutron fluxes worldwide, with a 4π emission rate of $\sim 1 \times 10^{11}$ neutrons per second from the target. For our experiment, we used a source intensity of 7×10^9 neutrons per second. The diode was positioned approximately 5 centimeters from the source, yielding a flux of about 2.23×10^7 n/cm² s. Fig. 2 shows the neutron source on the right and highlighted by a yellow rectangle on the left, the aluminum sample holder.

Six devices were irradiated: three with neutrons incident on the anode side and three on the cathode side. In both cases, the irradiations were performed at normal incidence (90°) to the device surface, carried out in successive steps.

During each run, the DUT was biased at a constant cathode voltage V_K. The cathode leakage current was continuously monitored and recorded by the SMU, while the current pulses from indirect ionization caused by nuclear-reaction products were collected by the oscilloscope. Each run was stopped either after $\sim 1.3 \times 10^8$ neutrons had impacted on the device (run time ~ 100 s) or when the leakage current exceeded a pre-defined compliance value of 105 µA. The compliance was set to this value, as it is the maximum current supported by the SMU, which guarantees optimal measurement accuracy across the supplied voltage range (up to 600 V). The choice of 1.3×10^8 neutrons ensured a reasonable probability of stimulating the nuclear reactions discussed in Section V. After irradiation, the DUT was electrically characterized to detect structural damage; if none was observed, the run was repeated at a higher cathode voltage.

IV. The Experimental Results

Experimental waveforms show a strong dispersion in regards to collected charge as the applied cathode voltage varies. Fig. 3 shows typical current pulses during neutron irradiation at increasing cathode bias voltage starting from $V_K = 350$ V to the critical value $V_K = 600$ V. The wave forms are plotted on two separate graphs because the largest pulse amplitude is nearly three orders of magnitude greater than the smallest. Fig. 4

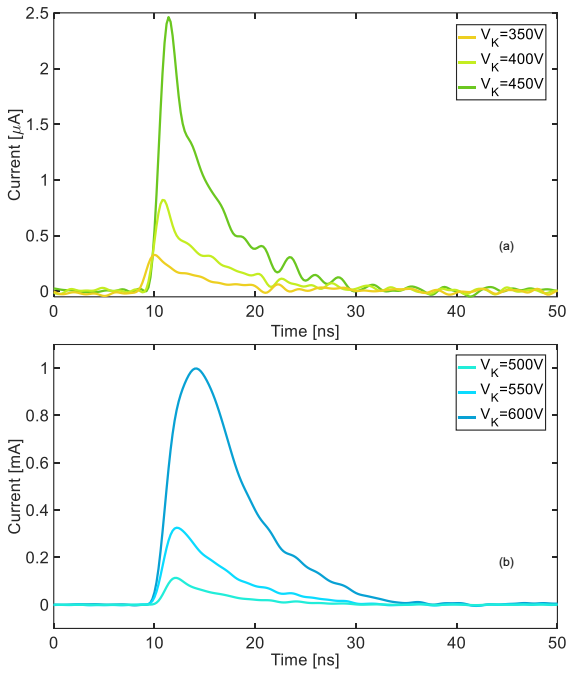

Fig. 3. A typical current pulses during neutron irradiation at cathode voltage equal to (a) 350 V, 400 V, and 450 V; (b) 500 V, 550 V, and 600 V.

shows the scatter plots of the events recorded during neutron irradiation under the same bias conditions as Fig.3(a). Each indirect ionization is represented in the scatter plot by a point. The abscissa corresponds with the current-pulse peak, while the ordinate represents the charge collected at the cathode terminal and generated by the interaction between the neutron secondary ionization and the electric field. The charge is calculated as the integral of the current pulse. As the bias voltage increases, the interaction between the ionizing secondary particles and the stronger electric field results in greater charge accumulation. As a result, the number of current pulses detected at the cathode terminal rises significantly. Assuming the same average neutron fluence per irradiation step, the recorded events increase from just a few hundred at $V_K = 350$ V to several thousand at $V_K = 600$ V.

Fig. 5 shows the scatter plot of events recorded during irradiation at a cathode $V_K = 600$ V. The inset highlights current pulses with longer rise times, marked in green shading. Two points, indicated by green and blue circles, were examined, and their corresponding pulses are displayed in Fig. 6. Although the two waveforms have the same area (20 pC), they exhibit different rise times, suggesting distinct charge-collecting mechanisms. Notably, these events appear only during irradiations at the critical voltage. Neutron-induced indirect ionization produces significant variability in charge distribution, spanning nearly three orders of magnitude.

Both the devices irradiated from the anode side and those from the substrate side exhibited the same burnout voltage, and a similar charge distribution generated at different bias voltages. Nuclear reactions in the surface metallization, passivation layers, heat sink, and substrate do not significantly contribute. Only the reactions occurring in the quasi-intrinsic region, where a strong electric field is present, generate currents capable of causing burnout. Because of the limited neutron energy, the

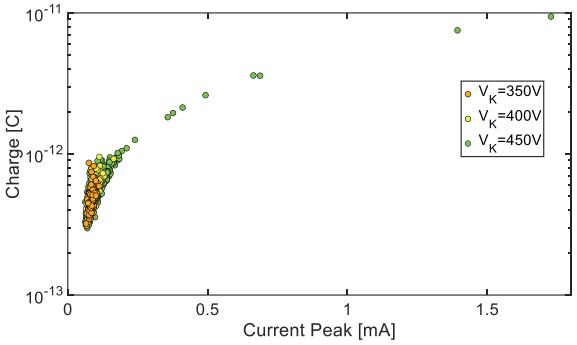

Fig. 4. Scatter plot of the events recorded during irradiations at different values of bias V_K: 350 V (orange circles), 400 V (yellow circles), and 450 V (green circles).

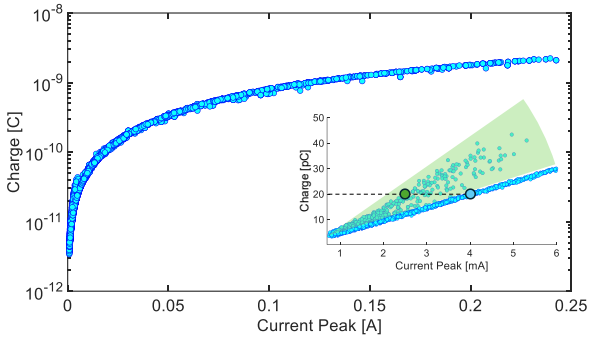

Fig. 5. Scatter plot of the events registered during irradiation at V_K = 600 V

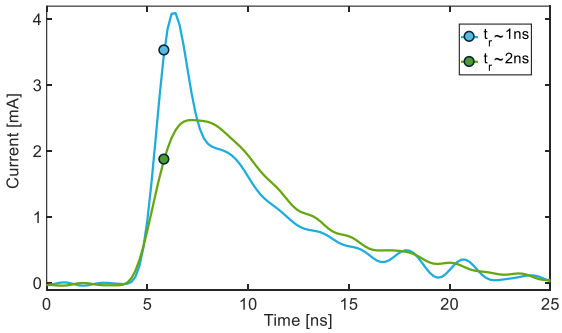

Fig. 6. The current pulse of the two equal charge events highlighted in the inset of Fig. 5 as the green and blue circles.

ranges of the heavy nuclear reaction products in the surface layers are too short to reach the quasi-intrinsic region, while light products such as protons and alphas deposit too little ionization energy in the active area to trigger significant effects.

All tested devices exhibited destructive failure at a cathode voltage of 600 V, demonstrating that even low-energy neutrons can cause damage to power devices. This failure was marked by a sudden increase in cathode leakage current, eventually reaching the compliance limit of the SMU. Fig. 7 shows the time evolution of the leakage current during neutron irradiation at V_K = 600 V: the cathode current exceeds the instrument compliance after ~ ten seconds, indicating a burnout event. Before the failure, no appreciable signs of degradation were observed; the current leakage value is comparable to that of a pristine devise.

The electrical characterization conducted after irradiation confirms the occurrence of the destructive event. Fig. 8

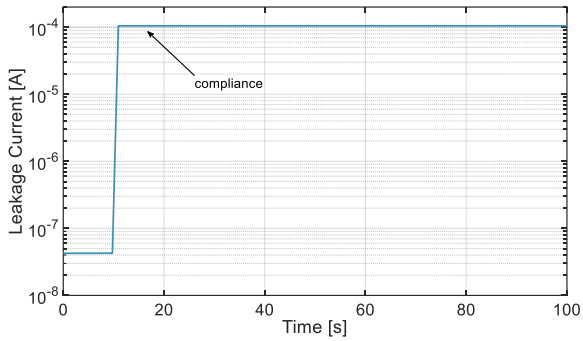

Fig. 7. Leakage current time evolution during irradiation at V_K = 600 V.

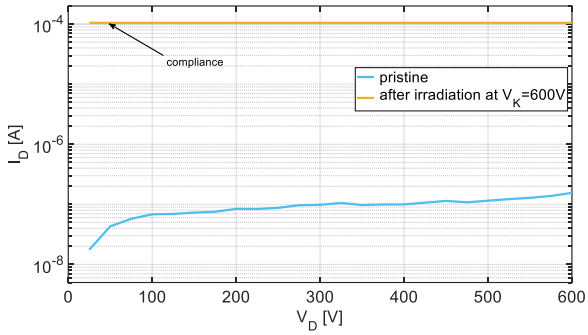

Fig. 8. Reverse diode characteristics: pristine device (blue curve) versus device irradiated with 14 MeV neutron at V_K = 600V (ochre curve).

illustrates a comparison between the reverse diode characteristics of the pristine device (blue curve) and those of the device after being irradiated at V_K = 600 V (yellow ochre curve). In the latter case, the leakage current reaches the compliance limit of the SMU, indicating junction breakdown associated with the burnout event.

The burnout is caused by a significant charge release during the ionization process. Neutrons induce indirect ionization by interacting with atomic nuclei in the device materials, producing charged particles and recoil nuclei. If these deposit sufficient charge by ionization within the device's sensitive volume, they can trigger a burnout event.

V. The Simulation Procedure

The experimental results were analyzed using finite element simulations with Silvaco TCAD tools. Three-dimensional electrothermal simulations, exploiting the cylindrical symmetry of the unit cell, were employed to investigate the failures caused by the ionizing secondary particles generated from 14 MeV neutron-induced in silicon.

The unit cell parameters were calculated using [19] and are consistent with those reported in other studies [20, 21]. In the second phase, these parameters were slightly adjusted to improve the agreement between the simulated and experimental breakdown curves.

Fig. 9 shows the schematic of the structure simulated in TCAD and the summarizes the key parameters of the structure itself. Fig. 10 shows the good overlap between the experimental curve (blue solid line) and the simulated curve (red dashed line).

A classical Selberherr model was used to implement impact ionization during the simulation.

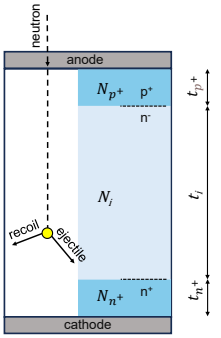

Parameter	Description	Value	Unit
N_{p^+}	Doping concentration anode region	$1 \cdot 10^{19}$	cm^{-3}
N_i	Doping concentration quasi-intrinsic region	$2.25 \cdot 10^{14}$	cm^{-3}
N_{n^+}	Doping concentration cathode region	$1 \cdot 10^{19}$	cm^{-3}
t_{p^+}	Depth anode region	10	µm
t_i	Depth quasi-intrinsic region	45	µm
t_{n^+}	Depth cathode region	10	µm

Fig. 9. Schematic and main technological parameters of the silicon PiN diode

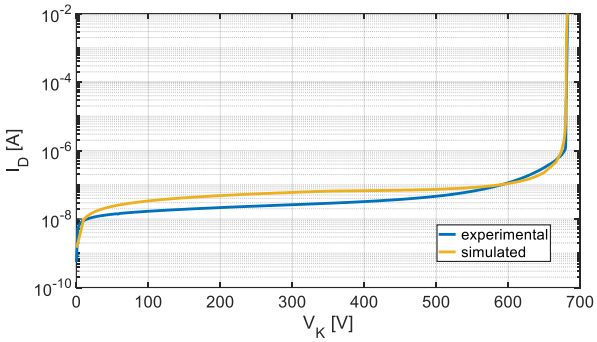

Fig. 10. Comparison between the experimental and simulated breakdown curve.

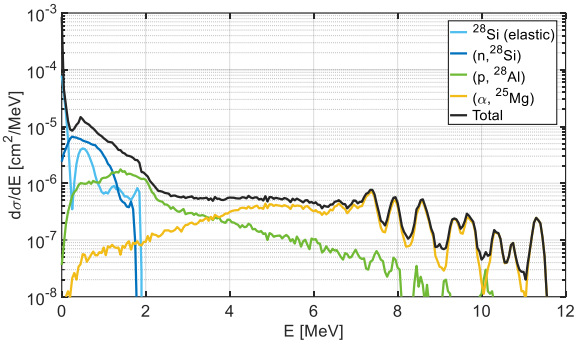

Fig. 11. Simulated energy spectrum response of our silicon diode when irradiated with 14 MeV neutrons. Simulated by using G4SEE [15].

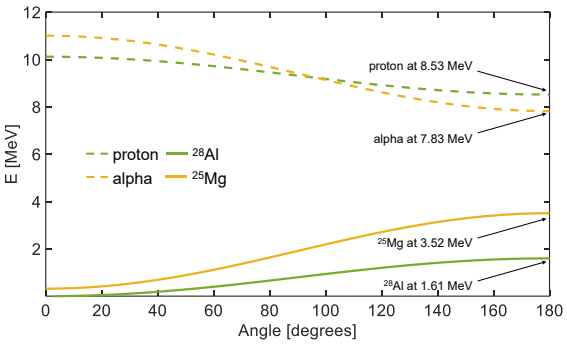

Fig. 12. The laboratory energy of the recoil (heavy) and ejectile (light) particles as a function of the relative ejectile emission angle in the center of the mass reference frame.

Neutron reactions with silicon can produce recoil nuclei and light particles, like protons or α-particles; the probability of these reactions depends on the neutron threshold energy. Nuclear reactions with dopants were neglected since, in the quasi-intrinsic region, the silicon atomic density is almost 5×10^{22}/cm^3, while the doping atomic density is approximately ~10^{14}/cm^3, and thus negligible.

To evaluate the energy deposition of secondary particles generated by 14 MeV neutrons interactions in the silicon diode, simulations were performed using the G4SEE toolkit. The fully depleted diode was modeled as a 2.5 mm × 2.5 mm × 400 μm silicon parallelepiped, with sensitive volume comprising a 10 μm-thick p$^+$-region and a 45 μm-thick n$^-$-region. The physics models of radiation-matter interactions and the threshold energy values for particle transport were defined as described in [22]. The monoenergetic neutron beam was defined as a Gaussian beam with a mean energy of 14 MeV and a standard deviation of 100 keV.

Fig. 11 shows the simulated energy-deposition spectrum of the silicon diode under 14 MeV neutron irradiation. Results are expressed as the differential cross-section distribution (dσ/dE), using an energy bin width of dE = 0.05 MeV.

The simulation indicates that the main reactions contributing to energy deposition in the diode are ^{28}Si(n, n$'$)Si below 1.5 MeV, ^{28}Si(n, p)^{28}Al between 1.5 MeV and 3.5 MeV, and ^{28}Si(n, α)^{25}Mg above 3.5 MeV.

For the given fluence (2.23×10^7 n/cm²), the expected number of reactions is:

- 17.3×10^3 for ^{28}Si(n, n)^{28}Si;
- 5.85×10^3 for ^{28}Si(n, p)^{28}Al;
- 1.21×10^3 for ^{28}Si(n, α)^{25}Mg.

These cross-section values were obtained from Projection Angular-momentum Coupled Evaporation (PACE4) [23, 24], a Monte Carlo code specifically designed to simulate fusion-evaporation nuclear processes.

Kinematic calculations indicate that the heavy reaction products ^{28}Si, ^{28}Al, and ^{25}Mg can recoil with energies up to approximately ~1.9 MeV, 1.6 MeV, and 3.5 MeV, respectively, while the energies of protons and alpha particles from these reaction channels can reach up to 10 MeV and 11 MeV, respectively. The low energy of heavy recoil nuclei results in very short ionization ranges; thus, only neutron reactions within the depletion region can trigger potential burnout. Fig. 12 shows the laboratory energy of the secondary particles as a function of the emission angle of ejectiles in the center-of-mass. For example, if a proton (or alpha) is emitted at 0º, the corresponding ^{28}Al (^{25}Mg) must be emitted at 180º to conserve momentum. To model neutron effects on SEEs, we analyze the ionization capabilities of nuclear-reaction products. High-energy ejectiles generally have long ranges and low LET, making the worst-case for localized energy deposition the maximum-energy heavy recoils (θ_{cm} = 180°).

Fig. 13 illustrates an example of the ^{28}Si(n, α)^{25}Mg nuclear reaction occurring within the diode. A neutron strikes the anode contact perpendicularly (dotted line), with nuclear reaction taking place in the quasi-intrinsic region. In the direction of neutron penetration, the initial electric field has a trapezoidal shape, as shown in the lower part of the figure. The two reaction products, moving in opposite directions, generate electron-hole plasma that interacts with the entire electric-field profile.

The energy released by the secondary particles shown in the Fig. 13 (blue curve) was calculated using the SRIM code [25]. The short ionization range of the heavy recoil nucleus indicates that potentially damaging neutron reactions occur in the depletion region. To identify the sensitive volume in our simulations, the quasi-intrinsic layer was discretized into ten points, considered as the sites generating the ionizing products.

Based on the results presented in Figures 11 and 12, we simulated the effects of the following ionizing species:

- proton at 8.53 MeV and ^{28}Al at 1.61 MeV;
- alpha at 7.83 MeV and ^{25}Mg at 3.52 MeV.

Additionally, for the scattered silicon ion, we selected two specific energy values aiming for a good compromise between energy and occurrence probability:

- ^{28}Si at 0.55 MeV;
- ^{28}Si at 1.1 MeV;

VI. The Simulation Results

Fig. 14 shows the simulated charge from various secondary particles collected at the cathode terminal from generated at different locations, with a cathode bias voltage of V_K = 550 V. The (α, ^{25}Mg) pair clearly produces a larger charge compared to the other secondary particles. As the generation site moves away from the depletion region, the collected charge gradually decreases. The only exception occurs for the (α, ^{25}Mg) couple, at the abscissa 60, where the generated alpha particle develops an ionization peak aligned with the electric-field maximum at the p^+/n^- interface. The electric-field peak is reduced by the presence of the intense electron-hole pair plasma, resulting in a significant current pulse.

Under the same bias condition that revealed the experimental failure, the combination of (α, ^{25}Mg) triggered burnouts, indicating a sensitive area in the depletion region near the p^+/n^- interface. Fig. 15 illustrates the simulated collected charge generated by the (α, ^{25}Mg) pair with a bias voltage of V_K = 600 V in the safe area. The figure also highlights, with a dashed background, the sensitive area where this causes burnout.

Fig. 16 shows a scatter plot comparing the events recorded during irradiation at V_K = 500 V, V_K = 550 V, and V_K = 600 V with simulations based on the selected ionizing secondary particles under the same voltage bias conditions. The simulation results closely match the experimental data, confirming the validity of our models. For the reaction products (p, ^{28}Al) and (α, ^{25}Mg), only the case with a relative angle of 180° was considered.

When the (α, ^{25}Mg) pair is generated between abscissas of 15 µm and 30 µm under a reverse bias voltage V_K = 600 V, the resulting ionization can trigger a thermal burnout. The electron-hole pairs released in the depletion region deform the original electric field distribution, shifting a secondary peak toward the n^-/n^+ interface. Fig. 17 (a) illustrates this rearrangement of the electric field shape after charge deposition.

Simultaneously, a significant impact ionization rate occurs along the alignment of secondary particles at both the p^+/n^- and n^-/n^+ interfaces, as shown in Fig. 17 (b). Carriers accelerated by the electric field generate additional electron–hole pairs in an

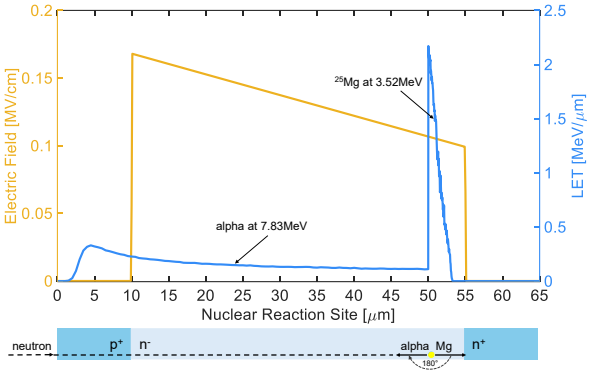

Fig. 13. Schematic of linear energy transfer (LET) induced by secondaries, with the alpha particle being emitted at 180°.

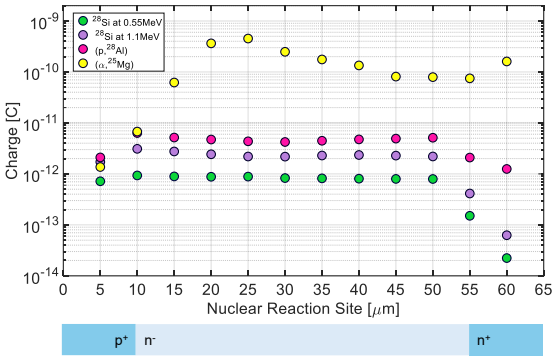

Fig. 14. Simulated collected charge induced by the different secondary particles at V_K = 550 V.

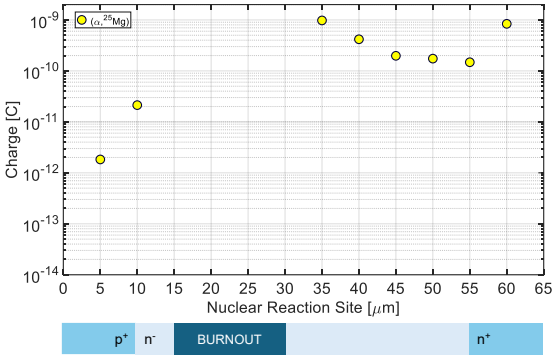

Fig. 15. Simulated collected charge induced by the (α, ^{25}Mg) couple at V_K = 600 V; the dashed area indicates the occurrence of burnout.

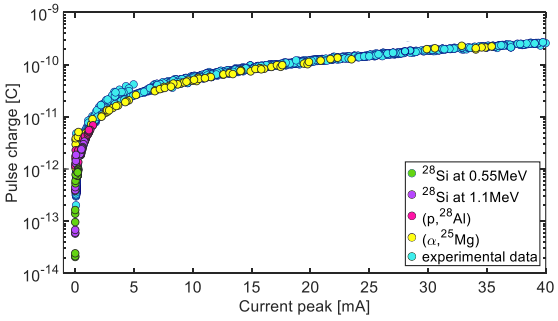

Fig. 16. Comparison of recorded events during irradiations and simulated current pulses regarding charge and peak.

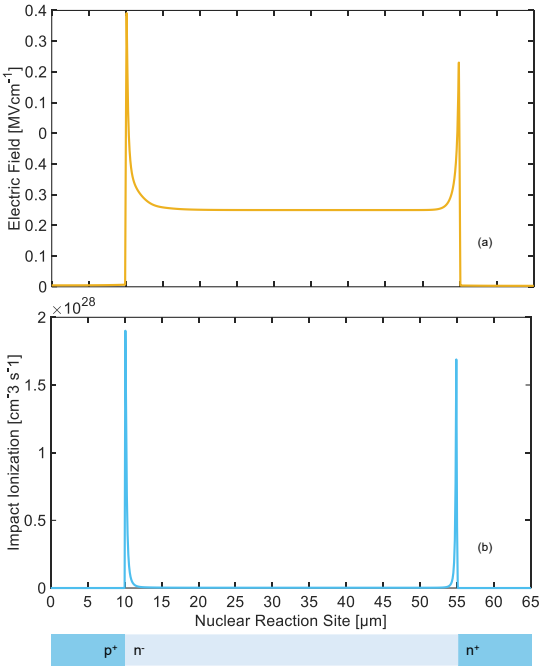

Fig. 17. Electric field (a) and impact ionization rate (b) distribution during the self-sustaining mechanism at the critical voltage V_K = 600 V

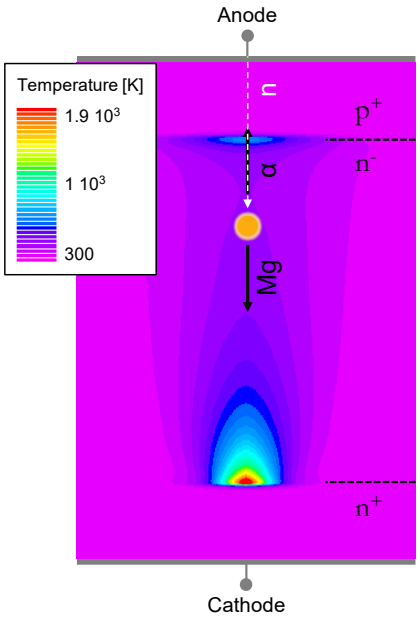

Fig. 18. Elementary cell thermal map.

iterative process. This process becomes self-sustaining if the accelerated carriers maintain a high impact ionization rate.

Consequently, neither the electric field nor the impact ionization rate relaxes to their initial distribution, and the process rapidly drives a large current density, leading to thermal burnout.

Fig. 18 shows the thermal map of the elementary cell activated by the self-sustaining mechanism. At the n^-/n^+ interface along the fragment alignment, the temperature exceeds the melting point of silicon, confirming the occurrence of burnout.

Let us examine the (n, alpha) reaction channel. Fig. 19 shows the electric-field distribution in the bias condition after only the

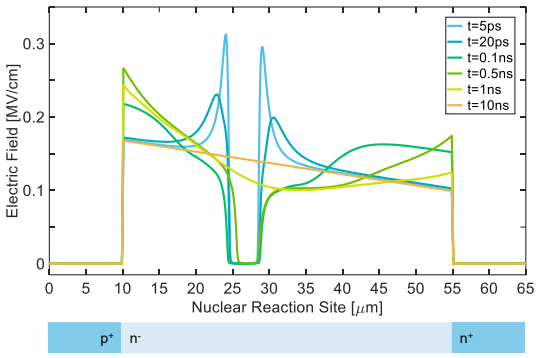

Fig. 19. Electric field distribution after deposition of ^{25}Mg in the sensitive area.

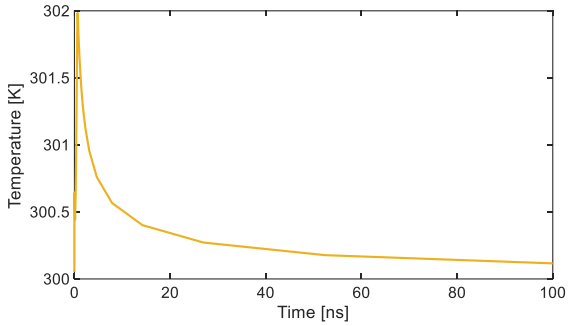

Fig. 20. Lattice temperature time evolution after deposition of ^{25}Mg in the sensitive area.

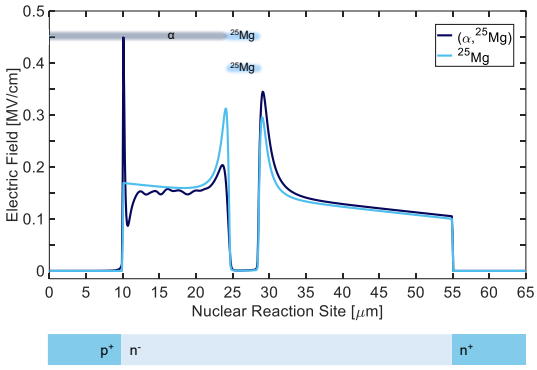

Fig. 21. Electric field distribution at 5 ps after deposition of ^{25}Mg, light blue curve, and (α,^{25}Mg), dark blue curve.

^{25}Mg energy deposition within the sensitive area. The high ionization capability of this heavy nuclear reaction product causes pronounced local depression of the electric field.

However, due to the magnesium's short ionization range, there is insufficient interaction with the full electric-field profile to trigger a burnout event. After a few nanoseconds, the electric field quickly returns to its original trapezoidal distribution (orange), and the lattice temperature, after a slight rise of a few kelvins, decays exponentially, as shown in Fig. 20.

Fig. 21 shows the electric-field distribution in the bias condition V_K = 600 V, at 5 ps after energy deposition by ^{25}Mg (light blue) and by the (α, ^{25}Mg) pair (dark blue). Unlike magnesium, the light alpha particle has weak ionization capability but a penetration range of tens of micrometers. Its ionization slightly deforms the electric field near the p^+ interface (dashed oval), raising the field at this interface to the critical value. Combined with the intense plasma deposited by

magnesium, this configuration leads to that shown in Fig. 17, initiating burnout. Individually, the two products of the neutron reaction induce negligible effects; together, however, they interact with the electric-field profile and deposit sufficient electron–hole plasma to trigger a catastrophic event. For the ^{25}Mg product alone to activate a destructive effect, the simulation indicates that its energy should be approximately 8 MeV; this value corresponds to an impacting neutron energy of around 30 MeV.

VII. Conclusion

Experimental results from an irradiation campaign at the FNG facility demonstrated that 14 MeV neutrons can induce thermal burnout in high-voltage power devices.

To investigate this failure mechanism in a power PiN diode, we developed a methodology combining experimentally recorded current pulses with electrothermal simulations driven by the energy deposition of the most probable nuclear-reaction fragments. The study reveals that the (α, ^{25}Mg) pair, when generated in the left half of the intrinsic region near the p^+/n^- interface at the critical bias voltage, can cause thermal burnout of the diode. The failure arises from a self-sustained process driven by the electric field and impact ionization.

Acknowledgements

The authors wish to acknowledge Dr. Mario Pillon and the staff of the FNG facility, ENEA, Frascati, for the precious support supplied during the irradiation campaigns.

References

[1] J. F. Ziegler, "Terrestrial cosmic rays," in *IBM Journal of Research and Development*, vol. 40, no. 1, pp. 19-39, Jan. 1996, 10.1147/rd.401.0019.

[2] D. L. Oberg, J. L. Wert, E. Normand, P. P. Majewski and S. A. Wender, "First observations of power MOSFET burnout with high energy neutrons," in *IEEE Transactions on Nuclear Science*, vol. 43, no. 6, pp. 2913-2920, Dec. 1996, 10.1109/23.556885.

[3] J. Baggio, D. Lambert, V. Ferlet-Cavrois, P. Paillet, C. Marcandella and O. Duhamel, "Single Event Upsets Induced by 1–10 MeV Neutrons in Static-RAMs Using Mono-Energetic Neutron Sources," in *IEEE Transactions on Nuclear Science*, vol. 54, no. 6, pp. 2149-2155, Dec. 2007, 10.1109/TNS.2007.910039.

[4] H. Asai *et al*., "Terrestrial Neutron-Induced Single-Event Burnout in SiC Power Diodes," in *IEEE Transactions on Nuclear Science*, vol. 59, no. 4, pp. 880-885, Aug. 2012, 10.1109/TNS.2012.2203145.

[5] T. Shoji, S. Nishida, K. Hamada and H. Tadano, "Observation and Analysis of Neutron-Induced Single-Event Burnout in Silicon Power Diodes," in *IEEE Transactions on Power Electronics*, vol. 30, no. 5, pp. 2474-2480, May 2015, 10.1109/TPEL.2014.2361682.

[6] A. Akturk *et al*., "Terrestrial Neutron-Induced Failures in Silicon Carbide Power MOSFETs and Diodes," in *IEEE Transactions on Nuclear Science*, vol. 65, no. 6, pp. 1248-1254, Jun. 2018, 10.1109/TNS.2018.2833741.

[7] M. Ahmed, C. Stankus, A. Yanguas-Gil, J. Hryn, S. A. Wender and K. Gunthoti, "Neutron Radiation Failure-in-time Test of 1200V and 1700V SiC Power Transistors," in *IEEE Radiation Effects Data Workshop (in conjunction with 2020 NSREC)*," Santa Fe, NM, USA, Dec. 2020, pp. 113-117, 10.1109/REDW51883.2020.9325843.

[8] K. Niskanen *et al*., "Neutron-Induced Failure Dependence on Reverse Gate Voltage for SiC Power MOSFETs in Atmospheric Environment," in *IEEE Transactions on Nuclear Science*, vol. 68, no. 8, pp. 1623-1632, Aug. 2021, 10.1109/TNS.2021.3077733.

[9] C. Peng, H. Zhang, Z. Zhang, T. Ma, Z. Wang and Z. Lei, "Comparison of 14-MeV Neutron-Induced Damage in Si and SiC Power MOSFETs," in *IEEE Transactions on Electron Devices*, vol. 72, no. 9, pp. 5104-5110, Sept. 2025, 10.1109/TED.2025.3588129.

[10] R. Ball *et al*., "Estimating Terrestrial Neutron-Induced SEB Cross Sections and FIT Rates for High-Voltage SiC Power MOSFETs," in *IEEE Transactions on Nuclear Science*, vol. 66, no. 1, pp. 337-343, Jan. 2019, 10.1109/TNS.2018.2885734.

[11] A. Hands, P. Morris, K. Ryden, C. Dyer, P. Truscott, A. Chugg, and S. Parker, "Single Event Effects in Power MOSFETs Due to Atmospheric and Thermal Neutrons," in *IEEE Transactions on Nuclear Science*, vol. 58, no. 6, pp. 2687-2694, Oct. 2011, 10.1109/TNS.2011.2168540.

[12] S. G. Alberton *et al*., "On the Vulnerability of UMOSFETs in Terrestrial Radiation Environments," in *IEEE Access*, vol. 13, pp. 53885-53894, March 2025, 10.1109/ACCESS.2025.3553758.

[13] A. Hands, P. Morris, C. Dyer, K. Ryden and P. Truscott, "Single Event Effects in Power MOSFETs and SRAMs Due to 3 MeV, 14 MeV and Fission Neutrons," in *IEEE Transactions on Nuclear Science*, vol. 58, no. 3, pp. 952-959, Jun. 2011, 10.1109/TNS.2011.2106142.

[14] A. Pietropaolo *et al,* "The Frascati Neutron Generator: A multipurpose facility for physics and engineering," *Journal Physics: Conf. Ser.*, vol. 1021, no. 1, pp. 012004, May 2018, 10.1088/1742-6596/1021/1/012004.

[15] D. Lucsányi, R. G. Alía, K. Biłko, M. Cecchetto, S. Fiore and E. Pirovano, "G4SEE: A Geant4-Based Single Event Effect Simulation Toolkit and Its Validation Through Monoenergetic Neutron Measurements," in *IEEE Transactions on Nuclear Science*, vol. 69, no. 3, pp. 273-281, March 2022, 10.1109/TNS.2022.3149989.

[16] Silvaco-Atlas Users Manual. Silvaco International. CA: Santa Clara; 2019.

[17] M. Martone, M. Angelone, and M. Pillon, "The 14 MeV Frascati neutron generator," *Journal of Nuclear Materials*, vol. 212–215, pp. 1661–1664, Sept. 1994, 10.1016/0022-3115(94)91109-6.

[18] M. Martone, M. Angelone, and M. Pillon, "Frascati neutron generator (FNG)," in *Proc. SPIE*, vol. 2339, pp. 208–213, March 1995, 10.1117/12.204156.

[19] B. J. Baliga, Fundamentals of power semiconductor devices, Springer Cham, Feb. 2019, 10.1007/978-3-319-93988-9.

[20] A. Shaker *et al.*, "Identification of power PIN diode design parameters: Circuit and device-based simulation approach," in *Ain Shams Engineering Journal*, vol. 12, no. 3, pp. 3141-3155, Sept. 2021, 10.1016/j.asej.2021.02.005.

[21] Shaohong Li, Long Zhang, Jing Zhu, Qingxi Tang, Ling Sun, Hao Wang, Xin Tong, Weifeng Sun, "A 600V PiN diode with partial recessed anode and double-side Schottky engineering for fast reverse recovery," in *Superlattices and Microstructures,*" vol. 128, pp. 56-66, Apr. 2019, 10.1016/j.spmi.2019.01.006.

[22] S. G. Alberton *et al*., "Single-Event Effects Induced by Monoenergetic Fast Neutrons in Silicon Power UMOSFETs," in *IEEE Transactions on Device and Materials Reliability*, vol. 25, no. 3, pp. 492-500, Sept. 2025, 10.1109/TDMR.2025.3572829.

[23] O.B.Tarasov, D.Bazin, "LISE++: Radioactive beam production with in-flight separators," Nuclear Instruments and Methods, " in *Physics Research Section B: Beam Interactions with Materials and Atoms*, vol. 266, no 19, pp. 4657-4664, Oct. 2008, 10.1016/j.nimb.2008.05.110.

[24] A. Gavron, "Statistical model calculations in heavy ion reactions," in *American Physical Society*, vol. 21, no. 1, pp. 230-236, Jan 1980, 10.1103/PhysRevC.21.230.

[25] J. F. Ziegler *et al*, "SRIM–The stopping and range of ions in matter (2010)," *Nuclear Instruments and Methods in Physics Research Section B: Beam Interactions with Materials and Atoms*, vol. 268, no. 11-12, pp. 1818-1823, Jun. 2010, 10.1016/j.nimb.2010.02.091.